Progress in Additive Manufacturing
https://doi.org/10.1007/s40964-021-00214-1

FULL RESEARCH ARTICLE

Powder spreading, densification, and part deformation in binder jetting additive manufacturing

Yousub Lee[1] · Peeyush Nandwana[2] · Srdjan Simunovic[1]

Received: 31 January 2021 / Accepted: 18 July 2021

Abstract

Binder jetting additive manufacturing (AM) can print complex structures in economical and scalable manner. Binder jetting AM comprises of deposition and weak binding of particles, known as green part, at room temperature and subsequent binder removal and sintering densification at high temperatures. However, during the densification (i.e., sintering), the part significantly deforms due to volume shrinkage. The deformation during sintering is difficult to predict, which prevents the widespread application of this technology. In this research, powder spreading simulation using discrete element method (DEM) was performed first to capture local variations in powder bed configuration. Second, finite element method (FEM) with a phenomenological continuum constitutive model was used to predict part shrinkage during the sintering process. DEM simulation showed variations in packing density, particle segregation, formation of uneven powder bed surface, and shift in particle size distribution (PSD). The sintering simulation modeled part deformation with a reasonable accuracy of 3% for solid-state sintering and intermediate liquid phase sintering. A demonstration case with non-uniform initial packing density showed that inhomogeneous green part density and PSD should be accounted for prediction of part deformation in binder jetting AM.

Keywords Binder jetting · Additive manufacturing · Powder spreading · Sintering deformation · Discrete element method · Finite element method · Particle segregation

1 Introduction

Binder jetting is a popular additive manufacturing (AM) process, formulated in ASTM F42 [1]. Binder jetting AM uses sequential steps of metal powder spreading and polymer binder deposition on the powder bed. The process is repeated for all layers comprising the object's volume. The entire powder bed is then heated at a temperature of 200 ºC in a curing oven to cure the polymer binder and bind the metal particles in the desired regions. After curing, the parts are carefully extracted from the powder bed. In this state, the parts are fragile and are referred to as "green" parts [2]. A green part density is typically 30–60% [3–5] of the ideal, metal material density, and it always requires post-processing steps such as sintering or infiltration to achieve 95% of the ideal density or above, particularly for metal components. Binder jetting AM offers several advantages compared to fusion-based AM, such as negligible thermal stresses, lack of textured microstructure, and a wide range of processible materials and powders [1, 6]. However, a wide application of binder jetting AM is hampered mainly due to low part density [3, 4] and anisotropic deformation during sintering [7].

The initial packing density of the powder bed is important since it determines the green part density that influences part densification, shrinkage, and distortion during sintering step [8, 9]. The packing density in the powder layer varies with the particle shape and size distribution, powder spreading, and binder saturation [7, 10]. Part characteristics also contribute to distortion, as part dimension, geometric features, and printing orientation are strongly influenced by powder spreading and binder saturation during the deposition [1]. Post-processing steps such as binder burn-out temperature, and sintering strategies determine part deformation during densification. Sintering temperature, holding time, and heat

✉ Yousub Lee
leey@ornl.gov

[1] Computational Sciences and Engineering Division, Oak Ridge National Laboratory, Oak Ridge, TN, USA

[2] Material Science and Technology Division, Oak Ridge National Laboratory, Oak Ridge, TN, USA

Journal : Large 40964 | Article No : 214 | Pages : 15 | MS Code : 214 | Dispatch : 23-7-2021

rate are the key controlling factors for achieving optimal densification and associated shrinkage and distortion within a part [11–15].

Experimental characterization of powder bed is typically limited to bulk scalar properties (e.g., packing density, PSD, and surface roughness) and to measurement resolution for local variation of the properties over the powder bed. For instance, the local density variations in the green part as a function of build height during binder jetting AM were reported by Stevens et al. [7]. A cylindrical hollow jar with a rounded bulge in the middle was printed using a binder jetting machine and then sintered under vacuum at 1000 °C for 100 h and held for 2 h at the same temperature. Density contour was plotted in vertical cross-section of the jar. It showed ~ 40–70% density range at the flat protrusions whereas ~ 70–100% at the center curve region. However, the localized measurement of green part density in three dimensions is laborious and provides limited information. Alternatively, numerical simulations can provide highly localized scalar properties (e.g., number of interparticle contacts and particle segregation) as well as tensorial properties (e.g., orientation of interparticle contacts, porosity distribution and connectivity) in addition of the bulk scalar properties.

Powder spreading in binder jetting is analogous to that in powder bed AM process. Numerous studies have reported to reveal powder-spreading mechanism and correlation to powder bed quality [16–24]. A pioneer powder-spreading simulation for AM application was developed by Parteli and Pöschel [16]. They investigated how the process conditions influence the powder bed quality in terms of the surface roughness and roller velocity. The work showed that higher roller velocity and larger particle size distribution (PSD) reduces packing density and uniformity of the surface roughness. Haeri et al. [17, 18] have performed powder-spreading simulation with non-spherical particles of Poly-Ether Ether Ketone (PEEK) polymer particles. Similarly, they found that lower translational velocity leads to improved quality of powder bed. Interestingly, in the work, particle shape segregation was observed for the rod shaped particles during powder spreading. Experimentally, Muniz-Lerma et al. [25] observed particle segregation across the powder bed of AlSi7Mg in laser powder bed fusion (L-PBF) process. Mindt et al. [26] observed the occurrence of particle segregation using discrete element method (DEM) in L-PBF process. As the particle-spreading progresses, the coarser particles remain at the end of the layer. The propensity of segregation increases as the spreading is repeated. Meier et al. [19, 20] developed powder-spreading model based on DEM including interactions of particle-to-particle and particle-to-wall. Emphasis of the study lies on the calibration and investigation of cohesion force and effect on particle stacking and powder layer characteristic. It showed that decreased particle size leads to inferior powder bed quality due to increased cohesiveness. Lee et al. [22] developed computationally efficient DEM simulation. Their approach enables modeling of multiple layers by minimizing/eliminating modeling of every layer. They showed that higher rake velocity drives PSD shift to finer region. Chen et al. [21] proposed powder-spreading mechanisms for PBF AM process. They identified three types of deposition mechanisms: (1) cohesion effect, (2) wall effect, and (3) percolation effect causing particle segregation. Yao et al. [23] investigated the effect of different powder-spreading conditions, PSD, and wall effect on powder bed quality. They found that increasing blade velocity, blade angle (up to 15°) and the gap height between substrate and recoater is beneficial for powder bed quality.

Unlike traditional powder metallurgy based on the pressure sintering, the interaction between powder and binder jetting recoater system leads to inhomogeneous packing density, anisotropic interparticle contact distribution, particle segregation, and lower green part densities [27, 28]. The correlation between powder spreading and sintering steps is often neglected in many binder jetting-related simulations and the green part density is assumed to be homogeneous for the sintering simulations. Ideally, the measured or calculated green part density should be used as an input for the sintering model. The powder spreading model can assess the property variations in the green part and use them in the sintering model to determine the extent of part shrinkage during sintering.

Numerous phenomenological sintering studies have been reported over past decades in traditional powder metallurgy and ceramic industry [14, 15, 29–31]. Two most popular phenomenological models were developed by Olevsky [13, 14] for pressureless sintering and by Abouaf [32] for hot isostatic pressing (HIP). The early phenomenological models did not account for the influence of diffusion related physical phenomena (i.e., grain boundary diffusion, plastic flow, surface diffusion, etc.) on the grain growth and sintering stress etc. Physical model was developed by Riedel [33] to consider various physical phenomena during sintering. Nguyen et al. [30] compared those three commonly used sintering models based on case studies for Al_2O_3. It concluded that the three models predict the macroscopic sintering with reasonable accuracy, but still the phenomenological models can be more easily implemented than the physical models which require extensive parameter determination. Molla et al. [34] proposed a multi-scale numerical approach for shape prediction during sintering. Kinetic Monte Carlo (KMC) model was used to predict shrinkage rate and inhomogeneous microstructure evolution in meso-scale. Then, it is coupled with the continuum theory through FEM simulation to solve the sintering shrinkage of bi-layers in macro-scale. Deng et al. [35] used Abouaf model [32] to predict the shrinkage of carbon anode during HIP in combination with DEM simulation. The particle filling was explicitly modeled

Journal : Large 40964 | Article No : 214 | Pages : 15 | MS Code : 214 | Dispatch : 23-7-2021

using DEM to capture initial powder density and its local distribution in a cylindrical capsule. FEM model was subsequently used to calculate the continuum-scale shrinkage. The results showed that the geometrical difference occurred at the top corners after HIPing is attributed to the difference of packing density distribution.

Relatively few publications address the prediction of part deformation in binder jetting AM. Still, many numerical models have focused on sintering shrinkage in continuum-scale without consideration of powder spreading step or assuming homogenous and uniform configuration. In this article, we present why the powder spreading should be incorporated into the part-scale simulation for shrinkage prediction. Two distinct particle- and part-scale models are implemented and provide example studies. The particle-scale model uses discrete element method (DEM) to resolve the motion of individual particles and their effect on the powder bed configuration. The part-scale model uses continuum finite element method (FEM) to model deformation of the green part during sintering. The variations of powder bed characteristics and properties were quantified across the build platform. The part deformation was predicted at four sintering temperatures and validated with experimental results. Lastly, we demonstrate using the examples, the changes in deformation behavior that results from variations in green part density, which highlights the importance of working towards better integrating the particle simulation with sintering simulation.

2 Experiments

ExOne M-Flex binder jet machine was used to deposit the H13 cube coupons using ExOne aqueous binder (BA005) whose chemical composition can be found in the literature [36]. Cubic coupons with 20.3 mm in edge length were printed using a binder saturation of 85% and 105%. For each binder saturation, eight coupons were printed in the center of the build platform. The measured green density was 3.97 g/cm^3 and 3.91 cm^3 for 85 and 105% saturation samples, respectively. The percent green density was calculated using theoretical density of H13 (7.75 g/cm^3) and is ~ 51.33 and ~ 50.49% for 85 and 105% saturation coupons, respectively. The PSD was measured using Morphologi G3 particle analyzer. The particle size is 13.6, 19.2, and 32.0 µm for D_{10}, D_{50}, and D_{90}, respectively. The layer thickness of 100 µm was used for the deposition. While the binder saturation can have noticeable impact on liquid formation, our effort is focused at capturing the deformation rather than the underlying sintering mechanism. Thus, the model does not account for the effect of binder saturation and subsequent liquid formation during sintering. The cubes were heated to 900 °C at a ramp rate of 10 °C/min and held for 3 h to burn-out the binder and equalize temperature throughout the geometry. Then, the coupons were heated to 1340, 1360, 1380, and 1400 °C at a ramp rate of 10 °C/min and held for 5 h to determine the extent of densification as a function of the peak sintering temperature. The binder burn-out and sintering were conducted as a single cycle in a custom vacuum furnace using graphite heating elements under vacuum level of 10^{-5} mTorr. The coupons subjected to furnace cooling by simply switching off the furnace and the average cooling rates were in the range of ~ 4–7 °C/h. The sintered parts were measured for dimensional changes along x-, y-, and z-directions to determine the shrinkage during sintering while Archimedes method was used for measuring the density of the coupons.

3 Numerical simulation

In this study, two different types of multi-physics code were implemented for particle- and part-scale simulation. Powder spreading simulation was performed first to capture local variations in powder bed configuration using discrete element method (DEM), LIGGGHTS [37]. Second, a phenomenological continuum constitutive model was performed to predict part shrinkage during the sintering process using finite element method (FEM), ABAQUS [38]. The particle properties (PSD) and process parameters, i.e., roller velocity and RPM (revolutions per minute), were used as an input for powder spreading simulation. Then, the green density and sintering parameters were incorporated into part deformation simulation to predict the part shrinkage. The overview and data flow between simulations are summarized in the flow chart as shown in Fig. 1. Note that the two simulations used in this study are loosely linked by the assumption of uniform green part density.

3.1 Governing equations and assumptions

3.1.1 Particle-scale simulation

The metal powder particles fabricated through gas atomization process are typically spherical, in the order of 10 µm particle size range [8]. During rapid movements of powder spreading, individual powder particles and the recoater system interact by friction, collision, and cohesive forces, and can lead to different macroscopic powder configurations. In DEM simulation of powder spreading, the particles are modeled as discrete elastic spheres. The DEM's algorithm determines the overlap between two particles and calculates contact force based on particle contact models [8, 39]. Total forces acting on the particles are contact normal force, contact shear force, gravitational acceleration force, and cohesion force. Contact shear force and relative rotation

Journal : Large 40964 | Article No : 214 | Pages : 15 | MS Code : 214 | Dispatch : 23-7-2021

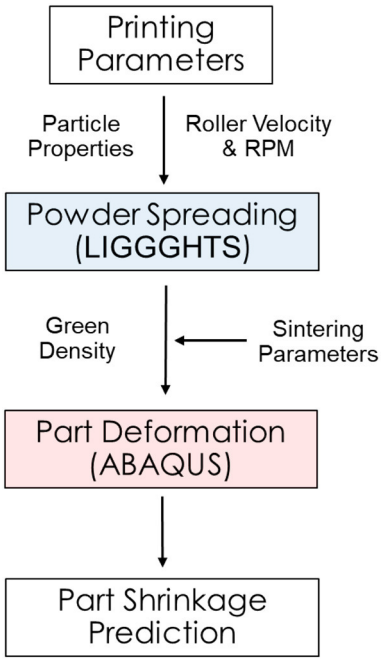

Fig. 1 Flow chart for binder jetting simulation, two simulation tools of LIGGGHTS and ABAQUS were used to understand correlation between powder spreading and part deformation

between two particles contribute to the momentum acting on the particles. The contact forces and momentum are used to calculate the translational and rotational acceleration based on Newton's second law of motion.

$$F_{\text{tot}} = F_{\text{cn}} + F_{\text{cs}} + F_{\text{g}} + F_{\text{a}} = m\ddot{x}, \tag{1}$$

$$M_{\text{tot}} = M_{\text{cs}} + M_{\text{r}} = I\dot{\omega}, \tag{2}$$

where F_{tot} is total force acting on a particle, F_{cn} is contact normal force, F_{cs} is contact shear force, F_{g} is gravitational force, m is particle mass, $\ddot{x}$ is acceleration velocity of particle, M_{tot} is total momentum acting on a particle, M_{cs} is momentum caused by shear force, M_{r} is rolling resistance, I is inertial of a particle, and $\dot{\omega}$ is angular acceleration of a particle.

In addition to the contact forces, cohesion forces, such as Van der Waals, metallic, and electrostatic force, are present between particles. For metal particles, electrostatic force is negligible with the size greater than 1 μm [8, 19, 20]. Van der Walls force is only effective in the order of 1 nm range. Moreover, metallic bonding might be much stronger than Van der Waals force in such a short-range order. The powder spreading typically occurs in atmospheric environment resulting in contamination, oxidation, and moisturization that affect the bonding between particles. Nevertheless, measuring all of the relevant adhesive forces is generally infeasible since the values vary by a couple of orders of magnitude depending on the particle surface conditions [19, 20, 40]. Adhesive normal forces, F_{a} in SJRK model is calculated using Eq. (3):

$$F_{\text{a}} = \kappa A, \tag{3}$$

where κ is the cohesion energy density and A is the contact area between sphere particles.

In this study, the simplified Johnson–Kendall–Roberts (SJKR) model. It models particle interaction using Hertzian theory with friction and cohesive energy. The DEM algorithms have been extensively described in the literature [8, 16, 19, 20, 39], so that only key features are discussed in this section.

3.1.2 Part-scale sintering simulation

Phenomenological model of Skorohod–Olevsky viscous sintering (SOVS) was used in this study to predict the shrinkage and deformation after sintering of the green part [13, 30, 41]. The SOVS model assumes incompressible nonlinear viscous deformation in porous media in which voids are uniformly distributed through the skeleton body called matrix. The matrix is the sum of the particles while the void is the sum of pores between particles. Although nonlinear viscous assumption may be more representative of the actual sintering behavior, acquisition of modeling parameters from the sintering experiments is considerably more difficult compared to the linear viscous model. Therefore, a linear viscous assumption has been broadly employed in the sintering process simulations [30] as well as in this study. The equivalent stress, σ_{eq} in the original SOVS constitutive model can be rewritten as a product of shear viscosity in the fully dense matrix phase, τ_0, and the equivalent strain rate,$\dot{\varepsilon}_{\text{eq}}$ in Eq. (4), which results in a simpler form of the general constitutive equation given by Eq. (5):

$$\sigma_{\text{eq}} = 2\tau_0\dot{\varepsilon}_{\text{eq}}, \tag{4}$$

$$\sigma_{ij} = 2\tau_0(\varphi\dot{\varepsilon}'_{ij} + \vartheta\dot{\varepsilon}'_{kk}\delta_{ij}) + \sigma_{\text{sin}t}\delta_{ij}, \tag{5}$$

where σ_{ij} is Cauchy stress tensor, φ is the normalized shear viscosity, $\dot{\varepsilon}'_{ij}$ is the deviatoric strain rate tensor, ϑ is the normalized bulk viscosity, $\dot{\varepsilon}'_{kk}$ is the trace of strain rate tensor, δ_{ij} is the Kronecker delta, and $\sigma_{\text{sin}t}$ is the sintering stress (=Laplace pressure).

The stress in Eq. (5) consists of a deviatoric and a volumetric part. The inversion of Eq. (5) provides the relationship between inelastic part of total strain rate (i.e., viscous sintering), the deviatoric and volumetric stresses.

Journal : Large 40964 | Article No : 214 | Pages : 15 | MS Code : 214 | Dispatch : 23-7-2021

$$\dot{\varepsilon}_{ij}^{ie} = \frac{\sigma_{ij}^{'}}{2\tau_0\varphi} + \frac{(\sigma_h - \sigma_{\text{sint}})\delta_{ij}}{3(2\tau_0\vartheta)} \quad (6)$$

where $\dot{\varepsilon}_{ij}^{ie}$ $(= \dot{\varepsilon}_{ij}^{\text{total}} - \dot{\varepsilon}_{ij}^{\text{elastic}})$ is the inelastic strain rate, $\sigma_{ij}^{'}$ is deviatoric stress tensor, and $\rho_h = (\rho_{kk}/3)$ is hydrostatic pressure.

Equation (6) gives a simple constitutive equation to describe sintering process. However, the shear viscosity φ and bulk viscosity ϑ are influenced by and vary with temperature, relative density, and grain growth during sintering. Also, sintering stress varies as a function of the relative density and grain radius. Shinagawa [42] incorporated grain growth factor into the viscosity term in SOVS model as an Arrhenius type function. The modified SOVS constitutive equation is expressed as in Eq. (7):

$$\dot{\varepsilon}_{ij}^{ie} = \frac{1}{2\tau_0\rho^{2n-1}}\left[\sigma_{ij}^{'} + \frac{2\delta_{ij}(\sigma_h - \sigma_{\text{sint}})}{9f_s^2}\right], \quad (7)$$

where $f_s(\rho)$ is $0.4/\sqrt{1-\rho}$. The sintering stress σ_{sint} is given as below:

$$\sigma_{\text{sint}} = \frac{2\gamma}{\omega R}\rho^m\left[\frac{\rho(1-\rho_0)}{\rho_0(1-\rho)}\right]^{\frac{1}{3}}, \quad (8)$$

where γ is the specific surface energy,ω is the correction factor for sintering stress, R is grain radius, m is the fitting constant for sintering stress, and ρ_0 is the initial green density. Note that the major parameters to control viscous sintering behavior are the effective shear and bulk viscosities and sintering stress which are functions of relative density, temperature and grain growth.

$$\tau_0 = C_1 T \exp\left(\frac{C_2}{T}\right) d^3, \quad (9)$$

$$d^j = d_0^j + \beta T, \quad (10)$$

$$G = \tau_0\rho^{2n-1}, \quad (11)$$

$$K = 3f_s^2\tau_0\rho^{2n-1}, \quad (12)$$

where C_1 and C_2 are material constant for viscosity, T is the temperature, d_0 is the initial grain size, j is exponent for grain growth, β is the constant for grain growth, and n is the exponential constant for shear and bulk viscosity modulus.

The evolution of relative density ρ can be calculated by the mass conservation and the inelastic strain rate, such that:

$$\frac{\dot{\rho}}{\rho} = -\dot{\varepsilon}_{kk}^{ie}, \quad (13)$$

$$\rho(\varepsilon) = \rho_0 \exp^{(-\varepsilon_{kk})}, \quad (14)$$

where $\dot{\rho}$ is the relative density evolution rate.

3.2 Boundary conditions

3.2.1 Particle size and distribution

The particle size and range of Co–Cr were obtained from measured values in literature [22]. The size range was between 25 and 105 µm. The D_{10}, D_{50}, and D_{90} are 29.84, 52.08, and 86.11 µm, respectively. The continuous particle size distribution was converted into discrete $D_{10} \sim D_{95}$ groups for the input of DEM simulation. Figure 2 shows particle size in cumulative size frequency and size frequency in radius and the converted particles used in the DEM simulation.

3.2.2 Modeling of powder spreading

The computational domain used to model the powder spreading is shown in Fig. 3. It consists of a roller, a spreading plate, and a build platform. The particles are spread by roller with a diameter of 5.62 mm. The roller moves at a fixed velocity of 5–125 mm and rotates in counter-clockwise at 150 and 300 RPM. The build platform has the dimensions of 6 mm (L) × 2 mm (W) × 0.28 mm (H). Approximately 40,000 particles are considered in the simulation. In author's previous work [22], the material properties for DEM was calibrated experimentally using static angle of repose (AOR) measurement and the simulation results agreed well with the optical observation of AOR. The particle properties are given in Table 1.

The cohesive energy density of Co–Cr can be converted to adhesive surface energy $\Delta\gamma$ of 0.053 mJ/m^2 using Eqs. 15 and 16. The detailed derivations are found in literature [22].

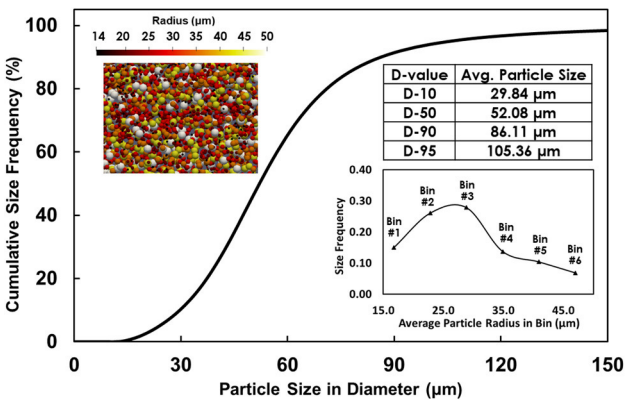

Fig. 2 Particle size in cumulative size frequency and size frequency in radius (inset at right bottom) and the converted particles in DEM simulation (inset at upper left)

Journal : Large 40964 | Article No : 214 | Pages : 15 | MS Code : 214 | Dispatch : 23-7-2021

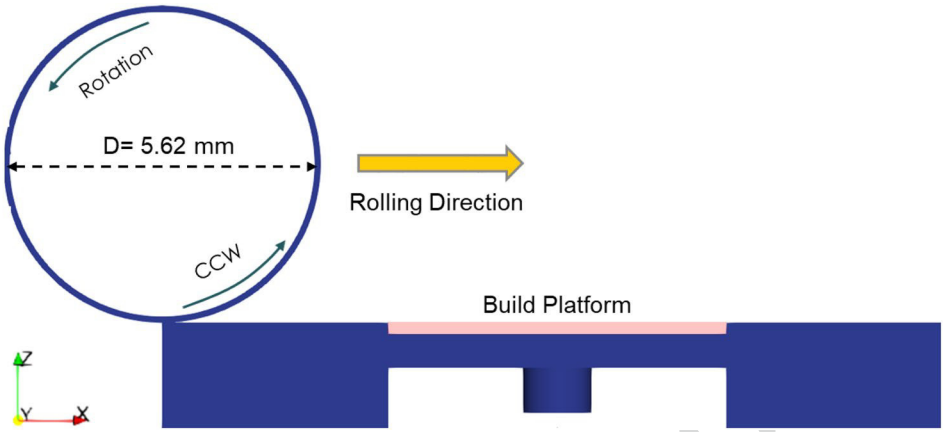

Fig. 3 Computational domain for powder spreading simulation

Table 1 Metal particle properties of Co–Cr used in DEM simulation [22]

Parameters	Symbol	Values	Unit
Particle density	ρ	7.75	g/cm^3
Gravity acceleration	G	981	cm/s
Poisson's ratio	N	0.33	–
Young's modulus	E	1.6×10^{10}	Pa
Cohesive energy density	κ	3.6×10^{7}	erg/cm^3
Restitution coefficient	Ω	0.4	–
Rolling friction coefficient	μ_r	0.05	–
Static friction coefficient	μ_s	0.4	–

The calculated value for $\Delta\gamma$ is close to the value of 0.02 mJ/m^2 for AOR = 29° and 0.06 mJ/m^2 for AOR = 34° found in the literature for Ti-6Al-4 V powder [19, 20].

$$\kappa = \sqrt[3]{\frac{8E*^2}{3R*\pi^2}}\sqrt[3]{\Delta\gamma} \tag{15}$$

or equivalently,

$$\Delta\gamma = \frac{3}{8}\frac{R*\pi^2}{E*^2}\kappa^3, \tag{16}$$

where and E^* represents the effective elastic contact modulus, R^* denotes the effective particle radius of the contact of two particles, and κ is cohesive energy density.

3.2.3 Part sintering simulation

The powder spreading stage creates a green density of 40–60% of the ideal. For a practical usage, the part density should be increased up to 95% and above. A commercial FEM code, ABAQUS was used for phenomenological sintering simulation. The thermal-stress analysis was sequentially coupled and presumed that the mechanical stress did not affect phase transformation and temperature evolution. The cubic geometry with 20.3 mm edge length in Fig. 4a was discretized by 68,921 hexahedron elements with DC3D8 and C3D8 types. SOVS model was implemented through UMAT user subroutine to predict the part shrinkage and deformation during sintering. Heating cycle of 3 h at 900 °C and 5 h at 1340 °C was implemented into the model with

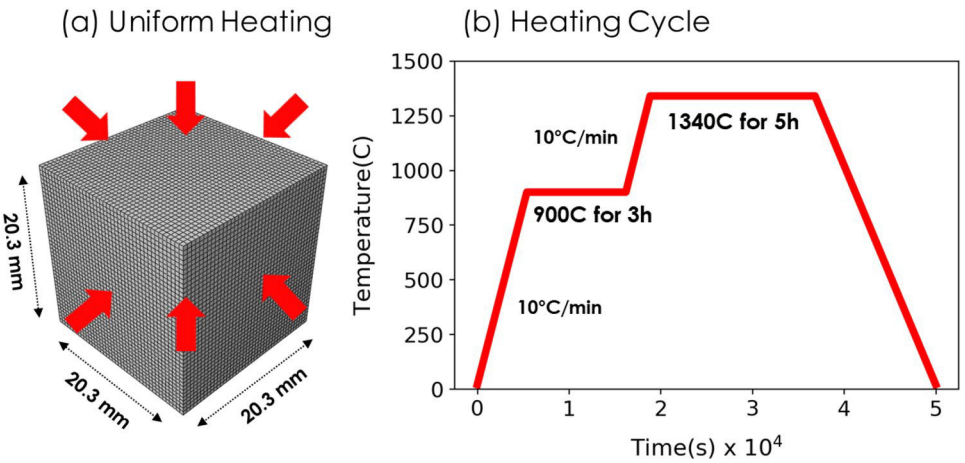

Fig. 4 Sintering conditions, **a** uniform heating applied to cube with 20.3 mm edge length and **b** heating cycle used for sintering simulation

Journal : Large 40964 | Article No : 214 | Pages : 15 | MS Code : 214 | Dispatch : 23-7-2021

variable amplitudes shown in Fig. 4b. The H13 material parameters used for SOVS model are given in Table 2.

Table 2 Material parameters of H13 used for sintering simulation

Parameters	Symbol	Values	Unit
Specific surface energy	γ	0.9	J/m^2
Material constant for viscosity	C_1	8.80×10^6	–
	C_2	5.96×10^3	–
Initial green density	ρ_0	50.3	%
Initial grain size	d_0	20	μm
Constant for sintering stress	m	5.0	–
Correction factor for sintering stress	ω	0.5	–
Exponent for grain evolution	j	1/0.37	–
Coefficient of grain evolution	β	6.0×10^{-6}	–
Exponential constant for bulk and hear modulus of viscosity	n	2.5	–

4 Results

4.1 Effect of process parameters on powder bed quality in a layer

Figure 5 shows the influence of roller velocity and RPM on powder bed density and surface roughness. Five roller velocities (5, 25, 50, 75, 100, and 125 mm/s) and two RPM s (150 and 300 RPM) were investigated in this work. The roller moves from the left to the right direction in the figure and revolves in counter-clockwise direction. The powder bed density is measured by the ratio of total volume of spheres in a virtual box to the volume of virtual box. Generally, the bed packing density decreases with increasing roller velocity and RPM. Notice that a hump starts to form at the velocity of 25 mm/s. The hump forms due to the interaction between particles and the printing hardware. For instance, the roller

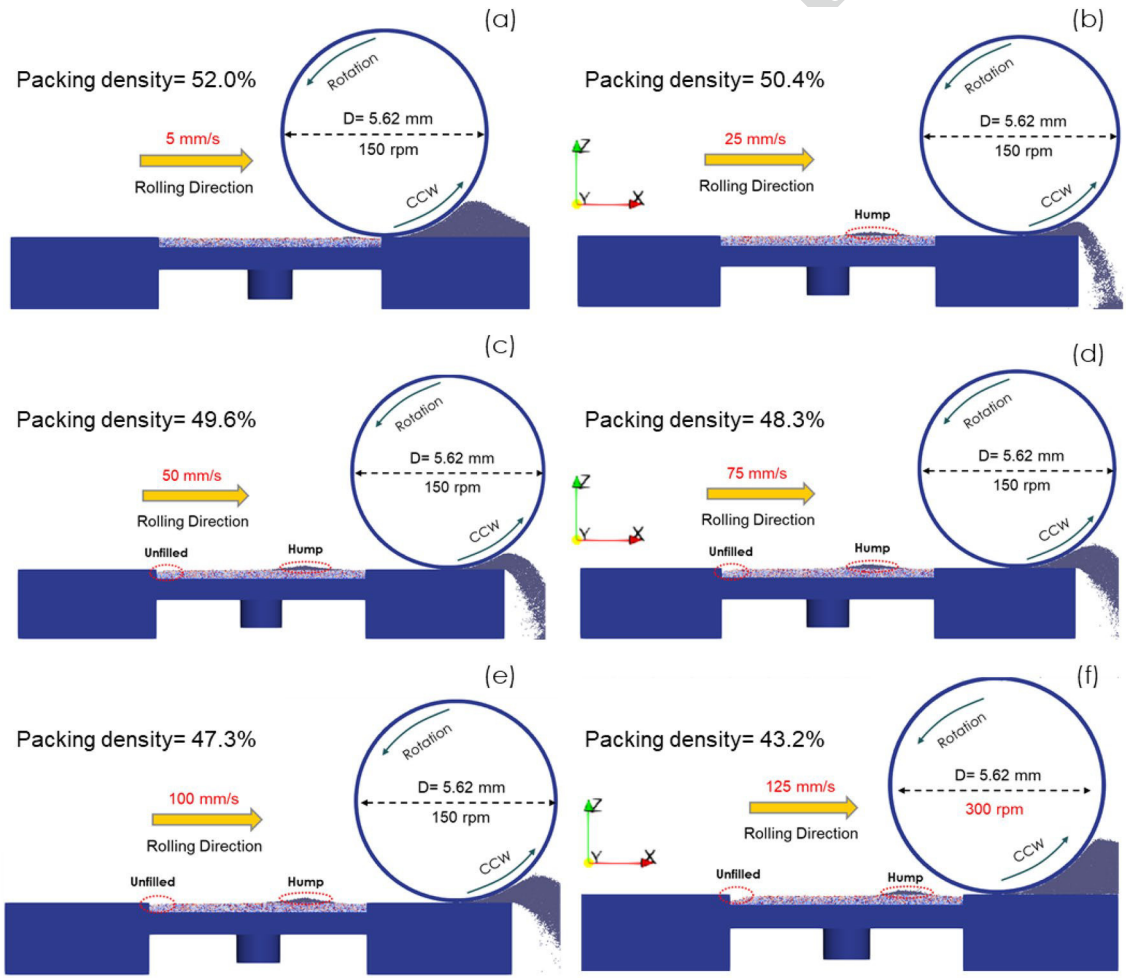

Fig. 5 Influence of roller velocity and RPM on powder bed density and surface roughness. 150 RPM + **a** 5 mm/s, **b** 25 mm/s, **c** 50 mm/s, **d** 75 mm/s, **e** 100 mm/s, and **f** 300 RPM + 125 mm/s. Note that the packing density decreases with roller velocity and RPM. Hump starts to form at the velocity of 25 mm/s

Journal : Large 40964 | Article No : 214 | Pages : 15 | MS Code : 214 | Dispatch : 23-7-2021

with counter-clockwise rotation continuously pushes the particles forward. Once they reach to the edge of the wall, reaction force caused by a contact between particles and the edge wall pushes the particles backward. Consequently, the hump forms close to the wall edge. Note that the pushing force is a combined form of linear and rotational motion.

The correlation of packing density with roller velocity and RPM is analyzed and shown in Fig. 3. Two kinds of packing density are conventionally used to compare the variation: (1) apparent packing density and (2) voxel packing density. The apparent density is defined by the ratio of total particle volume to box enclosure volume. The voxel density, which is theoretical quantity, is defined by the ratio of the total particle volume in an imaginary reference volume inside the packed particle to the reference volume. The voxel packing density is higher than the apparent density since it does not account for the wall effect. In this work, the apparent packing density is used to examine the effect of process conditions on the powder bed quality during the powder-spreading step. The box volume is marked as a light red color in Fig. 3.

The packing density linearly decreases with increasing the roller velocity and decreasing roller RPM. Two extreme velocities of 5 and 100 mm/s were first simulated, and a linear mathematical equation was derived from the two values (in blue color) shown in the Figure 6. The orange color denotes the packing densities which were subsequently predicted by simulations. The packing density values are close to the line based on the end conditions. This implies that we might use a linear relationship for further prediction of packing density at different roller velocities. In addition, double increased RPM of 300 was compared to RPM of 150 at the same roller velocity of 75 and 125 mm/s. It showed that the increased RPM decreases the packing density by 2.9% for both cases.

Surface quality is one of the key parameters of the powder bed quality. The powder bed surface quality is investigated for the considered process parameters. At 5 mm/s and 150 RPM in Fig. 7a, the surface appears smooth, and the bed area is tightly packed with the particles. As we increase the roller velocity, the surface becomes unleveled and the unfilled region in Fig. 7c–f starts to appear at the start and end edge of the bed. Higher roller velocity provides stronger translational forward motion to the particles and indicates that the translational motion is one of the reasons for the unfilled region at the start and end regions.

4.2 Particle segregation

Homogeneous PSD and uniform packing density would be preferred in the binder jetting process since inhomogeneities change binder infiltration and sintering kinetics [43]. Local variation of PSD potentially alters packing density and interparticle contacts in the powder bed leading to a different amount of binder saturation and heat conduction rate during sintering. Eventually, this result in non-uniform part deformation at the part level. Figure 8 shows the particles segregation occurring during the powder spreading process. Large fraction of coarser particles (in red color) are observed at the front area of roller in Fig. 8a. It implies that PSD may be different at the beginning and at the end of the powder bed layer as the spreading progresses. Particle segregation becomes weaker with increase of the roller velocity from 5 to 20 times. Higher rake velocity increases force in forwards and upwards leading to stronger mixing action at the rake front. As a result, particle segregation nearly disappears at higher rake velocity.

Particle size distribution at the roller front is further investigated in Fig. 9. Although the distribution generally resembles Gaussian shape, it shifts from positively skewed to negatively skewed as the roller velocity increases from (a) 5 mm/s, (b) 25 mm/s to (c) 100 mm/s. This PSD profile shows that the distribution is shifting from coarser to finer

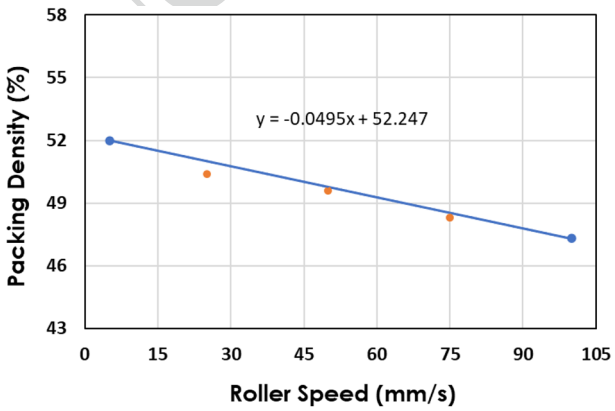

Process Parameters		Sim.	Regression
Speed (mm/s)	RPM	Density (%)	Density (%)
5	150	52.0	52.0
25	150	50.4	51.0
50	150	49.6	49.8
75	150	48.3	48.5
100	150	47.3	47.3
125	150	-	46.1
75	300	45.4	-
125	300	43.2	-

Fig. 6 Packing density proportionally decreases with roller velocity. Roller rotation shows further decrease of packing density

Journal : Large 40964 | Article No : 214 | Pages : 15 | MS Code : 214 | Dispatch : 23-7-2021

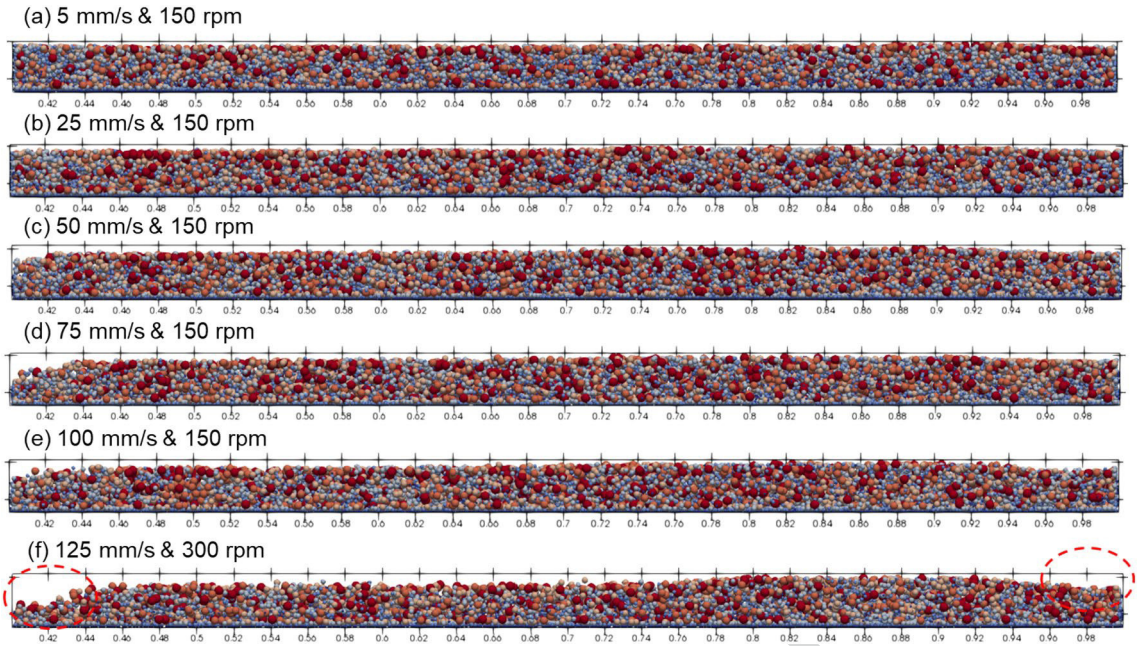

Fig. 7 Powder bed quality at the various roller velocity and RPM. **a** 5 mm/s and 150 RPM, **b** 25 mm/s and 150 RPM, **c** 50 mm/s and 150 RPM, **d** 75 mm/s and 150 RPM, **e** 100 mm/s and 150 RPM, and **f** 125 mm/s and 300 RPM. Higher roller velocity deteriorates the surface quality. Unfilled area is observed at the start and end of the powder bed

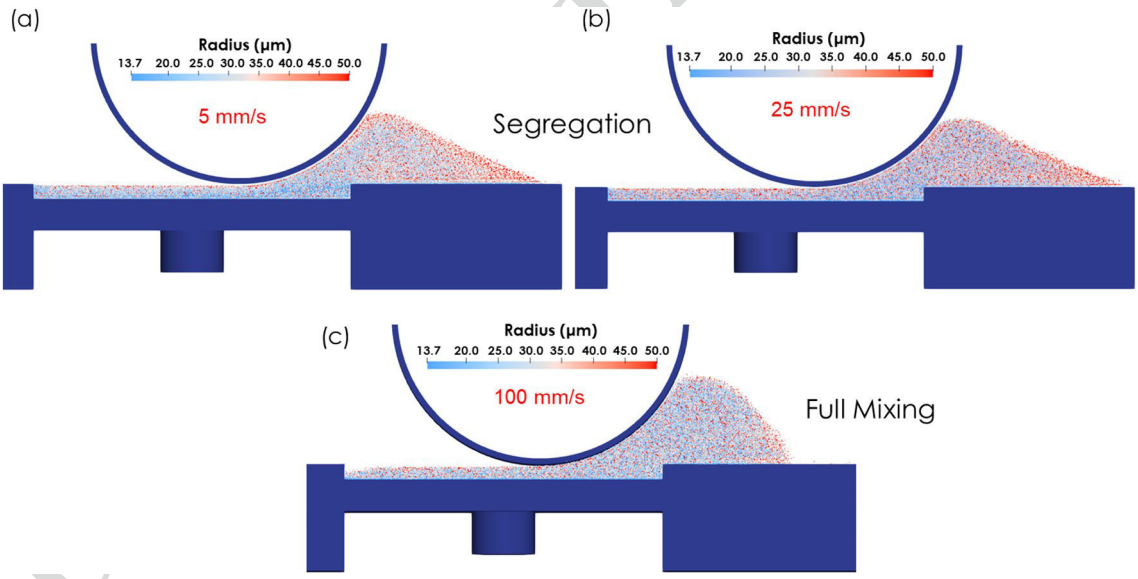

Fig. 8 Particles segregation at the roller front. Constant 150 RPM and roller velocity of **a** 5 mm/s, **b** 25 mm/s, and **c** 100 mm/s. Higher roller velocity reduces the particles segregation

particle region as the roller velocity increases. More fine particles are found at lower roller velocity of 100 mm/s.

The fractional change in each particle size range is summarized in Table 3. The particles range from 25 to 100 μm in diameter. Table 3 clearly shows that the fraction of fine particles continues to increase with increasing the roller velocity while the fraction of coarser particles decreases with increasing the velocity. As the roller velocity changes from 5 to 100 mm/s, the fraction of fine particles is increased by 10.1%. In other words, the fraction of coarser particles in bin 6 (=88 to 100 μm) is decreased

Journal : Large 40964 | Article No : 214 | Pages : 15 | MS Code : 214 | Dispatch : 23-7-2021

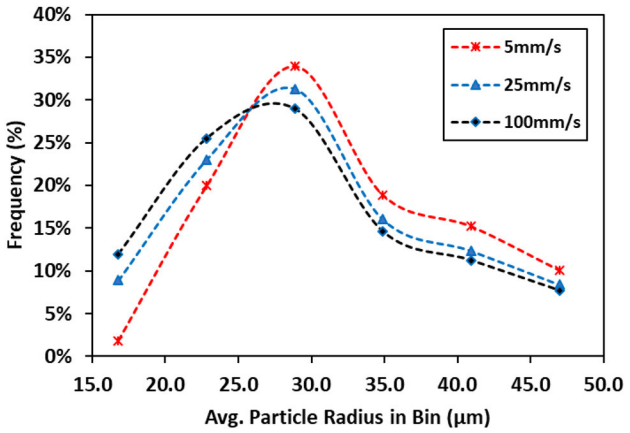

Fig. 9 Particle size distribution at the roller front in Fig. 8. The PSD profile shows that the distribution is shifting from coarser to finer particle as the roller velocity increases

by 2.4%. The migration of particles may have influence on packing density and sintering kinetics.

The particle segregation was reported in binder jetting AM literature [25, 27] where a periodic zone with finer and coarser particles was observed along the z-axis in the powder bed. The authors hypothesized that dynamic interaction between the counter-rotating roller and particles could lead to the particle segregation during spreading. Figure 10 shows how the roller velocity of 5 and 100 mm/s changes particle segregation in the powder bed. Finer particles settle at the lower bottom of the powder bed at 5 mm/s roller velocity in Fig. 10a while particles are fully mixed at 100 mm/s and uniform particle size distribution is observed at the lower and upper powder bed in Fig. 10b. Notice that for the 5 mm/s case, more fraction of coarser particles is found in the upper region than in the lower bottom region of the powder bed. This indicates that formation of the particle segregation is attributed to the roller spreading action [25]. Once the particles are spread for the next layer, the finer particles are placed above the coarser particles and consequently it generates a sandwich pattern with finer and coarser particle zones. This particle size fluctuation leads to local anisotropy in powder bed density. Moreover, for the same energy, the fine particles likely melt faster than the coarser particles due to smaller volume/mass ratio. It implies that the lower bottom region melts faster than upper region during sintering at above a certain temperature, which results in non-uniform part shrinkage. This suggests that particle segregation should be mitigated to achieve uniform final part properties and homogeneous distortion during sintering.

Table 3 Fractional change in particle size distribution at the roller velocity of 5, 25, and 100 mm/s

Bin	5 mm/s		25 mm/s		100 mm/s		ΔFraction (5 mm/s–25 mm/s)	ΔFraction (5 mm/s–100 mm/s)
	#Particle	Fraction	#Particle	Fraction	#Particle	Fraction		
1	245	1.8%	1351	8.9%	1881	12.0%	7.0%	10.1%
2	2646	20.0%	3492	23.0%	4008	25.5%	3.0%	5.5%
3	4503	34.0%	4752	31.3%	4553	29.0%	− 2.7%	− 5.0%
4	2502	18.9%	2434	16.0%	2294	14.6%	− 2.9%	− 4.3%
5	2017	15.2%	1878	12.4%	1765	11.2%	− 2.9%	− 4.0%
6	1337	10.1%	1278	8.4%	1211	7.7%	− 1.7%	− 2.4%
Sum	13,250	100.0%	15,185	100.0%	15,712	100.0%	–	–

The fraction of fine particles increases with increasing the roller velocity

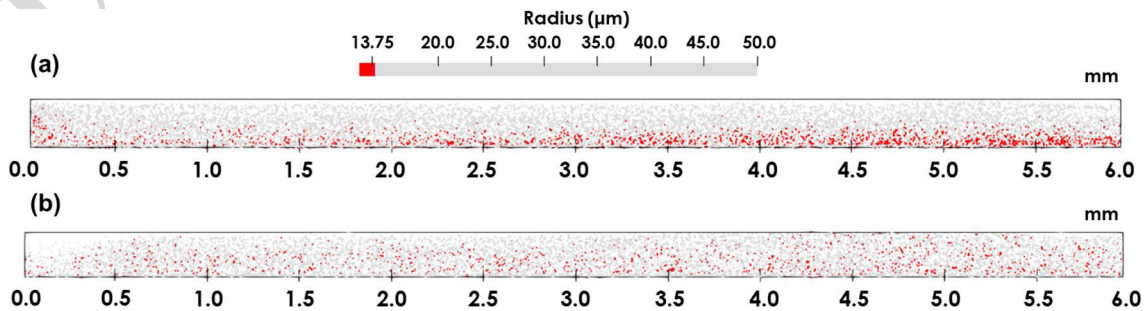

Fig. 10 Particle segregation in the powder bed. Blue and red indicate coarse and fine particles in radius, respectively. **a** 5 mm/s and **b** 100 mm/s

Journal : Large 40964 | Article No : 214 | Pages : 15 | MS Code : 214 | Dispatch : 23-7-2021

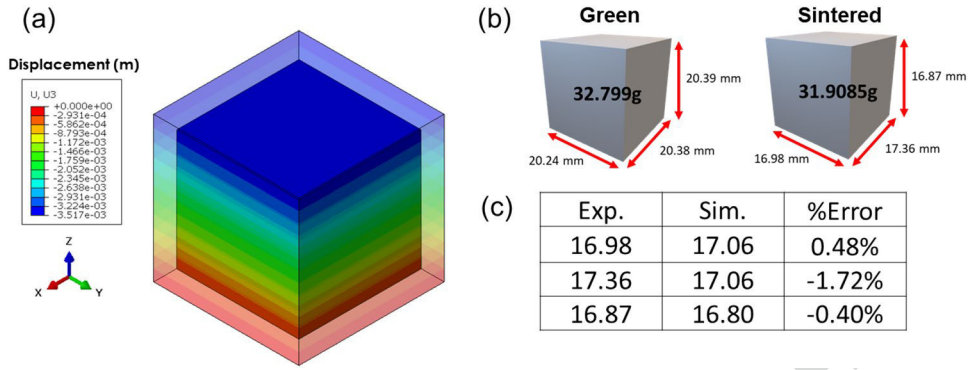

Exp.	Sim.	%Error
16.98	17.06	0.48%
17.36	17.06	-1.72%
16.87	16.80	-0.40%

Fig. 11 Predicted part shrinkage for the cube shape. The part shrinks about 3 mm in x-, y-, and z-directions. The phenomenological model predicts the shrinkage within minor error

4.3 Part deformation

Part shrinkage was simulated using continuum FEM model. The cubic sample has dimensions of 20.3 mm × 20.3 mm × 20.3 mm in the green part state prior to densification. The part was uniformly shrunk by 16% at all edges after sintering. Figure 11a shows the shrinkage in the FEM model along z-direction in comparison of original with sintered geometry. The dimensional change of the cube in green and sintered part is illustrated in Fig. 11b. About 3 mm shrinkage in all three directions occurred during sintering at 1340 °C. The simulation predicts the shrinkage with less than 0.5% error in y- and x-direction but 1.7% in y-direction in Fig. 11c. The results show that the phenomenological simulation reasonably well predicts the part shrinkage for the simple cube geometry.

Table 4 compares the predicted part deformation to the measured dimensions along x-, y-, and z-axes. The simulation predicts the deformation within approximately 3% at the temperature ranges of 1340–1380 °C. However, it underpredicts the shrinkage about by 15% at 1400 °C. The same underprediction is found at 1400 °C in the prediction of relative density in Table 5. The part deformation during sintering is a complex function of liquid volume fraction, the number of interparticle contact, powder bed configuration and initial particle size. A small volume of liquid starts to form at 1360 °C and increases the volume to 15% at 1400 °C due to chemical composition of the material. The shape loss at 1400 °C can be attributed to liquid phase sintering. Thus, the prediction error can be minimized by considering liquid phase sintering.

Anisotropic dimensional variation during sintering is a critical issue in part design aspect since the final part dimension is approximated in priori as CAD shape by STL (stereolithography) file. The anisotropic shrinkage is strongly related to non-uniform green part density and geometry related sintering conditions. Non-uniform green part density can be originated from inappropriate parameters settings during deposition and/or complex part geometry. The uniform green part density may not be maintained wherein segregation or PSD shift is present as shown in Figs. 8, 9, and 10 and Table 3. Thus, we used three demonstration cases to show how the heterogeneity in packing density changes the part deformation behavior during sintering. The packing density of 61% on the top and 64% on the bottom were set for the sintering simulation as shown in Fig. 12a. The flipped densities in Fig. 12b and low corner density in Fig. 12c were additionally tested. Notice that the part bends up, down, and even twisted toward the lower packing density

Table 4 Comparison of the predicted part deformation to the experiment after sintering in *x*-, *y*- and *z*-directions at various sintering temperatures

Temperature (°C)	Direction	Experiment (mm)	Prediction (mm)	Error (%)
1340	X	16.98	17.06	0.48
	Y	17.36	17.06	− 1.72
	Z	16.87	16.80	− 0.40
1360	X	16.58	17.03	2.70
	Y	16.89	17.03	0.81
	Z	16.35	16.79	2.69
1380	X	17.23	17.01	− 1.31
	Y	16.49	17.01	3.12
	Z	16.65	16.79	0.82
1400	X	16.65	16.87	1.35
	Y	17.27	16.87	− 2.29
	Z	14.49	16.64	14.83

Table 5 Comparison of the predicted relative density to the experiment after sintering

Temperature (°C)	Experiment	Prediction	Error (%)
1340	0.828	0.811	− 2.05
1360	0.896	0.831	− 7.25
1380	0.885	0.849	− 4.07
1400	1.000	0.853	− 14.90

Journal : Large 40964 | Article No : 214 | Pages : 15 | MS Code : 214 | Dispatch : 23-7-2021

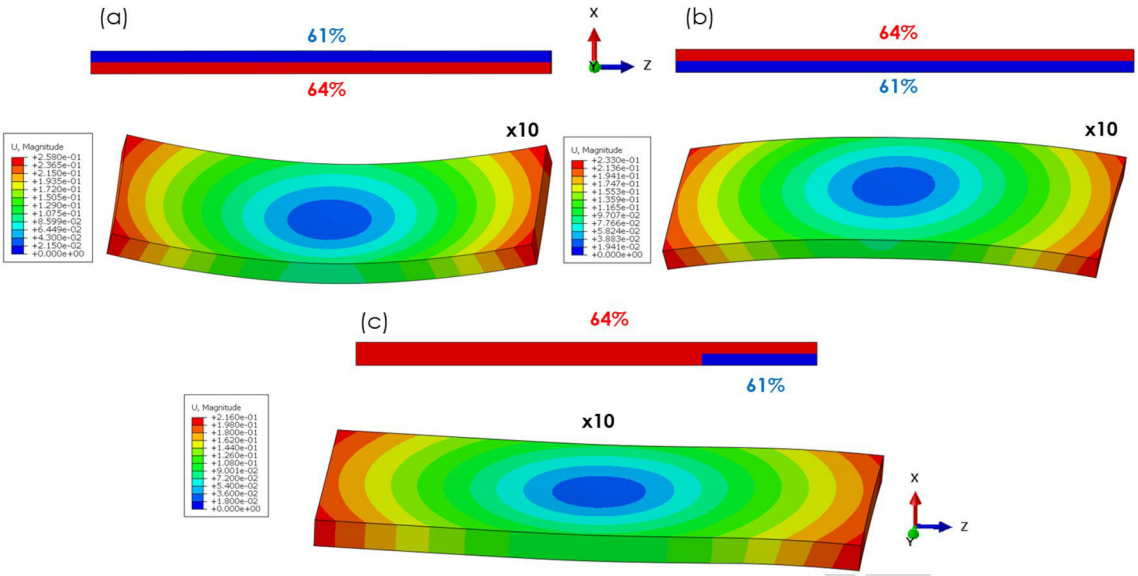

Fig. 12 The effect of non-uniform packing density on part distortion. Non-uniformity in green part density potentially leads to anisotropic part distortion in the part (the deformation is magnified by a scale factor of 10)

region. It indicates that inhomogeneous green part density potentially leads to anisotropic part distortion and that initial green part density should be taken into account, possibly by DEM simulations, and incorporated into continuum FEM sintering simulation for better prediction. Although the part was not printed to prove this concept, a prior literature [34] showed that the bi-layer plate bends towards a region with lower packing density due to difference in sintering rate that supports our findings. Total displacement is magnified by a scale factor of ten for better graphical representation.

5 Discussion

The powder spreading makes noticeable changes in the powder bed configuration. The packing density varies with the spreading parameters such as roller translational and rotational velocities. Surface related defects such as voids and humps were observed at the ends of powder bed layers. Particles migrate towards the bottom region of the powder bed resulting in vertical particle segregation. The roller velocity shifts the PSD. The segregation and PSD shift potentially influence the sintering rate and consequently leads to anisotropic part distortion [34, 43, 44].

In binder jetting AM literature, an enhanced linear shrinkage was observed in z-direction. This can be attributed to gravity and the rigidity of the powder bed configuration. The weight of upper layer applies a load to the lower layer during sintering. During sintering, the liquid binder filling the pore between particles will burn-out, and in particular the binder at the layer interface will disappear and the upper layer will collapse down to fill the void space where binder previously existed. The effect can be worse if the layer surface is unleveled as shown in Fig. 7. The amount of binder is not same to fill the hump and valley and consequently it results in irregular shrinkage in z-direction.

It is well known in powder metallurgy and binder jetting AM that the sintering shrinkage and densification are significantly influenced by the PSD and the green part density [2, 9]. For instance, PSD of wide (16–63 µm), fine (16–25 µm), and coarse (53–63 µm) produced green part density of 52, 45, and 48%, respectively. Typically, the densification is faster for lower green densities than for the higher ones. As seen in Figs. 8, 9, and 10, higher roller velocity shifts the PSD from coarser to finer region and causes the fine particle segregation at the bottom of the powder bed. The fine particle can contain more amount of liquid binder due to lower packing density. The effect can be repeated at the interface of every layer. During burn-out, more shrinkage in z-direction can occur in parts with segregated particles. The microstructure evolution such as grain size is affected by PSD, as well. The coarsening rate is related to the number of interparticle contacts that typically increase with packing density and the sintering rate is a function of the initial number of interparticle contacts [7, 45].

A significant shape loss in z-direction was observed at the sintering temperature of 1400 °C as shown in Tables 4 and 5. It is an indication of change of the sintering mechanism from solid-state to liquid phase sintering. According to thermodynamic prediction for H13, the liquid starts to form at 1360 °C and reaches the volume to 15% at 1400 °C. The sintering temperature range can be categorized into

Journal : Large 40964 | Article No : 214 | Pages : 15 | MS Code : 214 | Dispatch : 23-7-2021

three stages of solid-state sintering (1340–1360 °C), intermediate liquid phase sintering (1360–1380 °C), and liquid phase sintering (1380–1400 °C). The current model made a reasonable prediction up to the intermediate temperature range. It implicates that the solid-state sintering assumption is still effective under 15% or less liquid volume fraction. The current sintering prediction accounts for grain growth. However, the microstructure evolution during liquid phase sintering is more complicated due to orders of magnitude faster diffusion rate in liquid which results in lower accuracy of the part dimension and density prediction at 1400 °C.

The part deformation control in complex geometries is mostly based on trial and error by operators due to lack of linkage between process steps of green part formation and sintering. Several literature has reported the influence of printing conditions on particle flow, packing density, surface roughness, and void formation in AM field [16, 20, 23, 26]. Additionally, many literature has reported in continuum-scale sintering in powder metallurgy [30, 35]. However, the process optimization effort has been made in discrete fields of powder spreading and powder metallurgy not in integrated scheme. The correlations between the powder spreading and sintering processes in binder jetting AM have scarcely considered in the same pipeline. The particle segregation, PSD shift, non-uniform green part density in Figs. 8, 9, and 10, and resulting complex part deformation in Fig. 12 indicate that tight coupling of particle-scale DEM and continuum-scale FEM simulation should be made for binder jetting AM to improve the predictions in part deformation. The relationship is summarized in the Fig. 13. A detailed density distribution can be further applied to the part deformation model using voxel or representative volume element (RVE) at each integration point of the elements in the part deformation model.

6 Summary and conclusions

Particle-scale DEM and part-scale FEM simulations were used to investigate correlations between powder spreading and sintering deformation for binder jetting AM. The DEM provided a detailed information of powder bed structure such as packing density, particle segregation, surface roughness, and PSD in various process conditions. The results showed that higher roller velocity is recommended for forming homogeneous PSD (i.e., less or no particle segregation) over the powder bed. However, the higher roller velocity deteriorates the powder bed surface roughness. It creates unfilled edges and unleveled surfaces during the spreading. Different PSDs were observed at the beginning and end of the powder bed while the segregation becomes weaker with increase of the roller velocity. Larger fraction of fine particles was observed at the bottom of the powder bed.

Part deformation during sintering was predicted using continuum FEM model. The model provided a reasonable accuracy within 3% error in geometric dimension and part densification at the temperature ranges of 1340–1380 °C. However, the shrinkage was underpredicted in z-direction

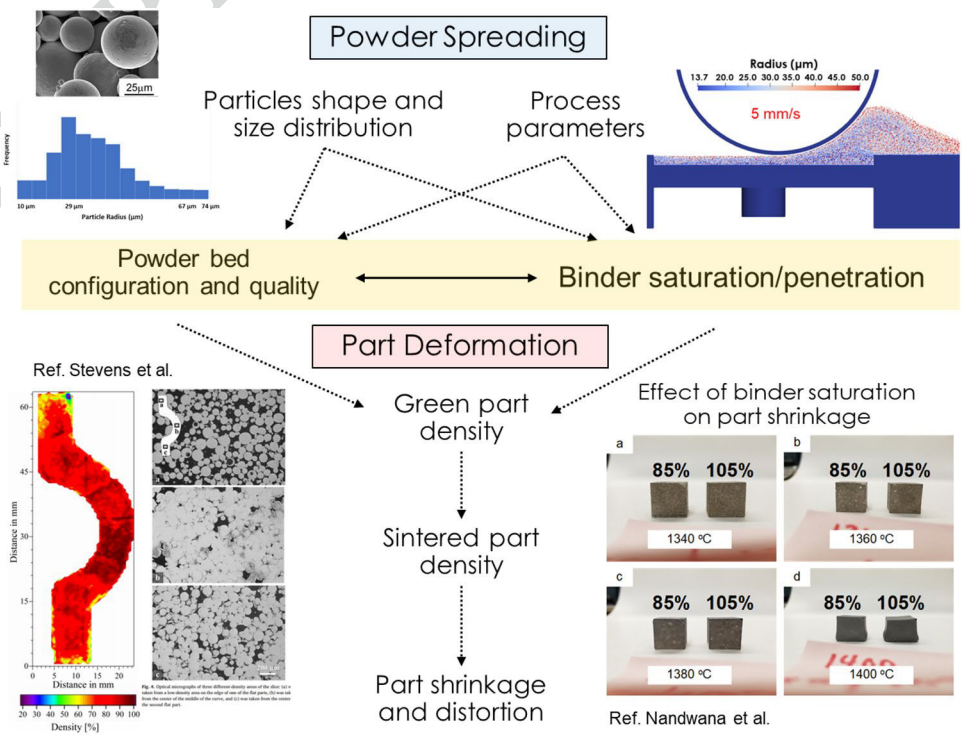

Fig. 13 Flow chart for binder jetting simulation. Powder spreading and sintering simulation should be coupled to improve the prediction accuracy at local region of the part [7, 46]

Journal : Large 40964 | Article No : 214 | Pages : 15 | MS Code : 214 | Dispatch : 23-7-2021

at 1400 °C due to the assumption of solid phase sintering. Green part density can vary with the spreading conditions and part geometry. The effect of inhomogeneous density was demonstrated in rectangular plate having a density of 61% and 64% at the top and bottom of the plate. The results showed that up, down, and twisted bending toward the low density regions. This indicates that small local variation in green part density can lead to anisotropic part deformation such that initial green part density needs to be accounted for in sintering simulation for improved predictions.

In current state of the work, DEM and FEM models are not explicitly coupled so that it only shows the reasons why the powder spreading should be incorporated into the continuum model. The local distribution of the green part density can be statistically quantified through micro-CT measurements with image analysis or computer vision. These data can be used for validation of the particle-scale model. The kinetic parameters such as densification rate can be obtained from in-situ measurements in the sintering furnace or by calibrated meso-scale simulations. Then, the prediction accuracy and full coupling of DEM and FEM model will be achieved in the desired level suggesting initial part geometry design for less trials and errors.

Acknowledgements This manuscript has been authored by UT-Battelle, LLC under Contract No. DE-AC05-00OR22725 with the U.S. Department of Energy. Research was co-sponsored by the U.S. Department of Energy, Office of Energy Efficiency and Renewable Energy, Advanced Manufacturing Office (AMO) and Vehicle Technologies Office (VTO) Propulsion Materials Program. This research used resources of the Compute and Data Environment for Science (CADES) at the Oak Ridge National Laboratory, which is supported by the Office of Science of the U.S. Department of Energy under Contract No. DE-AC05-00OR22725. The authors thank Dr. Sebastien N. Dryepondt for helpful support in preparation of this manuscript.

Author contributions Conceptualization, YL, PN, and SS; modeling, YL; data curation, YL; data analysis, YL and PN; writing–original draft, YL; writing–review and editing, PN and SS.

Declarations

Conflict of interest There is no conflict of interest associated with this publication.

Ethical approval This article does not contain any studies with human participants or animals performed by any of the authors.

Consent for publication The manuscript has been read and approved by all authors listed on the manuscript. This manuscript has been authored by UT-Battelle, LLC under Contract No. DE-AC05-00OR22725 with the U.S. Department of Energy. The United States Government retains and the publisher, by accepting the article for publication, acknowledges that the United States Government retains a non-exclusive, paid-up, irrevocable, world-wide license to publish or reproduce the published form of this manuscript, or allow others to do so, for United States Government purposes. The Department of Energy will provide public access to these results of federally sponsored research in accordance with the DOE Public Access Plan (http://energy.gov/downloads/doe-public-access-plan).

References

1. Parab ND, Barnes JE, Zhao C, Cunningham RW, Fezzaa K, Rollett AD, Sun T (2019) Real time observation of binder jetting printing process using high-speed X-ray imaging. Sci Rep 9(1):1–10
2. Nandwana P, Elliott AM, Siddel D, Merriman A, Peter WH, Babu SS (2017) Powder bed binder jet 3D printing of Inconel 718: Densification, microstructural evolution and challenges*. Curr Opin Solid State Mater Sci 21(4):207–218
3. Rishmawi I, Salarian M, Vlasea M (2018) Tailoring green and sintered density of pure iron parts using binder jetting additive manufacturing. Addit Manuf 24:508–520
4. Wheat E, Vlasea M, Hinebaugh J, Metcalfe C (2018) Sinter structure analysis of titanium structures fabricated via binder jetting additive manufacturing. Mater Des 156:167–183
5. Li M, Du W, Elwany A, Pei Z, Ma C (2020) Metal binder jetting additive manufacturing: a literature review. J Manuf Sci Eng 142(9):090801
6. Sufiiarov V, Polozov I, Kantykov A, Khaidorov A (2020) Binder jetting additive manufacturing of 420 stainless steel: densification during sintering and effect of heat treatment on microstructure and hardness. Mater Today. https://doi.org/10.1016/j.matpr.2020.01.144
7. Stevens E, Schloder S, Bono E, Schmidt D, Chmielus M (2018) Density variation in binder jetting 3D-printed and sintered Ti-6Al-4V. Addit Manuf 22:746–752
8. Lee Y, Nandwana P, Zhang W (2018) Dynamic simulation of powder packing structure for powder bed additive manufacturing. Int J Adv Manuf Technol 96(1–4):1507–1520
9. Mostafaei A, Rodriguez De Vecchis P, Nettleship I, Chmielus M (2019) Effect of powder size distribution on densification and microstructural evolution of binder-jet 3D-printed alloy 625. Mater Des 162:375–383
10. Miyanaji H, Orth M, Akbar JM, Yang L (2018) Process development for green part printing using binder jetting additive manufacturing. Front Mech Eng 13(4):504–512
11. Fang ZZ, Paramore JD, Sun P, Chandran KR, Zhang Y, Xia Y, Cao F, Koopman M, Free M (2018) Powder metallurgy of titanium—past, present, and future. Int Mater Rev 63(7):407–459
12. Nosewicz S, Rojek J, Wawrzyk K, Kowalczyk P, Maciejewski G, Maździarz M (2019) Multiscale modeling of pressure-assisted sintering. Comput Mater Sci 156:385–395
13. Olevsky EA (1998) Theory of sintering: from discrete to continuum. Mater Sci Eng R Rep 23(2):41–100
14. Olevsky EA, Tikare V, Garino T (2006) Multi-scale study of sintering: a review. J Am Ceram Soc 89(6):1914–1922
15. Abdelhafeez A, Essa K (2016) Influences of powder compaction constitutive models on the finite element simulation of hot isostatic pressing. Proc CIRP 55:188–193
16. Parteli EJ, Pöschel T (2016) Particle-based simulation of powder application in additive manufacturing. Powder Technol 288:96–102
17. Haeri S, Wang Y, Ghita O, Sun J (2017) Discrete element simulation and experimental study of powder spreading process in additive manufacturing. Powder Technol 306:45–54
18. Haeri S (2017) Optimisation of blade type spreaders for powder bed preparation in additive manufacturing using DEM simulations. Powder Technol 321:94–104
19. Meier C, Weissbach R, Weinberg J, Wall WA, Hart AJ (2019) Modeling and characterization of cohesion in fine metal powders

with a focus on additive manufacturing process simulations. Powder Technol 343:855–866
20. Meier C, Weissbach R, Weinberg J, Wall WA, Hart AJ (2019) Critical influences of particle size and adhesion on the powder layer uniformity in metal additive manufacturing. J Mater Process Technol 266:484–501
21. Chen H, Wei Q, Zhang Y, Chen F, Shi Y, Yan W (2019) Powder-spreading mechanisms in powder-bed-based additive manufacturing: Experiments and computational modeling. Acta Mater 179:158–171
22. Lee Y, Gurnon AK, Bodner D, Simunovic S (2020) Effect of particle spreading dynamics on powder bed quality in metal additive manufacturing. Integr Mater Manuf Innov 9:410–422
23. Yao D, An X, Fu H, Zhang H, Yang X, Zou Q, Dong K (2020) Dynamic investigation on the powder spreading during selective laser melting additive manufacturing. Addit Manuf. https://doi.org/10.1016/j.addma.2020.101707
24. Han Q, Gu H, Setchi R (2019) Discrete element simulation of powder layer thickness in laser additive manufacturing. Powder Technol 352:91–102
25. Muñiz-Lerma JA, Nommeots-Nomm A, Waters KE, Brochu M (2018) A comprehensive approach to powder feedstock characterization for powder bed fusion additive manufacturing: a case study on AlSi7Mg. Materials 11(12):2386
26. Mindt HW, Megahed M, Lavery NP, Holmes MA, Brown SGR (2016) Powder bed layer characteristics: the overseen first-order process input. Metall Mater Trans A 47(8):3811–3822
27. Jacob G, Jacob G, Brown CU, Donmez A (2018) The influence of spreading metal powders with different particle size distributions on the powder bed density in laser-based powder bed fusion processes. US Department of Commerce, National Institute of Standards and Technology
28. Zielinski J, Vervoort S, Mindt H-W, Megahed M (2017) Influence of powder bed characteristics on material quality in additive manufacturing. BHM Berg Hüttenmännische Monatshefte 162(5):192–198
29. Argüello JG, Reiterer MW, Ewsuk KG (2009) Verification, Performance, Validation, and Modifications to the SOVS Continuum Constitutive Model in a Nonlinear Large-Deformation Finite Element Code. J Am Ceram Soc 92(7):1442–1449
30. Van Nguyen C, Sistla SK, Van Kempen S, Giang NA, Bezold A, Broeckmann C, Lange F (2016) A comparative study of different sintering models for Al_2O_3. J Ceram Soc Jpn 124(4):301–312
31. Bordia RK, Kang SJL, Olevsky EA (2017) Current understanding and future research directions at the onset of the next century of sintering science and technology. J Am Ceram Soc 100(6):2314–2352
32. Abouaf M, Chenot J, Raisson G, Bauduin P (1988) Finite element simulation of hot isostatic pressing of metal powders. Int J Numer Methods Eng 25(1):191–212
33. Riedel H, Blug B (2000) A comprehensive model for solid state sintering and its application to silicon carbide, Multiscale deformation and fracture in materials and structures. Springer, Berlin, pp 49–70
34. Molla TT, Bjørk R, Olevsky E, Pryds N, Frandsen HL (2014) Multi-scale modeling of shape distortions during sintering of bi-layers. Comput Mater Sci 88:28–36
35. Deng Y, Herzog S, Kaletsch A, Broeckmann C, Horenkamp K, Huber G, Davies S, Marmottant A, Laurent V (2018) DEM and FEM simulation of powder filling and HIP in the production of HIP-clad inert electrodes. Euro PM 2018 Conference, European Powder Metallurgy Association (EMPA), Shrewsbury, UK
36. Saito T, Elliott AM (2019) Indirect additive manufacturing process. US Patent 15/783,574
37. Kloss C, Goniva C, Hager A, Amberger S, Pirker S (2012) Models, algorithms and validation for opensource DEM and CFD–DEM. Prog Comput Fluid Dyn 12(2–3):140–152
38. SIMULIA (2017) Abaqus analysis user's guide. Dassault Systémes, Providence
39. Stershic A, Simunovic S, Nanda J (2015) Modeling the evolution of lithium-ion particle contact distributions using a fabric tensor approach. J Power Sources 297:540–550
40. Escano LI, Parab ND, Xiong L, Guo Q, Zhao C, Fezzaa K, Everhart W, Sun T, Chen L (2018) Revealing particle-scale powder spreading dynamics in powder-bed-based additive manufacturing process by high-speed x-ray imaging. Sci Rep 8(1):15079
41. Cox N (2018) Modeling shape distortion of 3-D printed aluminum oxide parts during sintering, University of Pittsburgh
42. Shinagawa K (1999) Micromechanical modelling of viscous sintering and a constitutive equation with sintering stress. Comput Mater Sci 13(4):276–285
43. Bai Y, Wagner G, Williams CB (2017) Effect of particle size distribution on powder packing and sintering in binder jetting additive manufacturing of metals. J Manuf Sci Eng. https://doi.org/10.1115/1.4036640
44. Zago M, Lecis NFM, Vedani M, Cristofolini I (2021) Dimensional and geometrical precision of parts produced by Binder Jetting process as affected by the anisotropic shrinkage on sintering. Addit Manuf. https://doi.org/10.1016/j.addma.2021.102007
45. German RM (2014) Coordination number changes during powder densification. Powder Technol 253:368–376
46. Nandwana P, Kannan R, Siddel D (2020) Microstructure evolution during binder jet additive manufacturing of H13 tool steel. Addit Manuf. https://doi.org/10.1016/j.addma.2020.101534